Contents lists available at ScienceDirect

Physica Medica

Original paper

MRI-based numerical modeling strategy for simulation and treatment planning of nanoparticle-assisted photothermal therapy

Mohamadreza Asadi[a], Jaber Beik[a], Reza Hashemian[b], Sophie Laurent[c], Ali Farashahi[a], Mehri Mobini[d], Habib Ghaznavi[e,*], Ali Shakeri-Zadeh[a,*]

[a] Medical Physics Department, School of Medicine, Iran University of Medical Sciences (IUMS), Tehran, Iran
[b] US Oncology Inc., Cincinnati, OH, USA
[c] General, Organic and Biomedical Chemistry, NMR and Molecular Imaging Laboratory, University of Mons, Mons, Belgium
[d] Department of Mathematics, Faculty of Mathematics, University of Sistan and Baluchestan, Zahedan, Iran
[e] Zahedan University of Medical Sciences (ZaUMS), Zahedan, Iran

A B S T R A C T

Nanoparticle-assisted photothermal therapy (NPTT) has recently emerged as a promising alternative to traditional thermal therapy methods. Computational modeling for simulation and treatment planning of NPTT seems to be essential for clinical translation of this modality. Non-invasive identification of nanoparticle distribution within the tissue is a key perquisite for accurate prediction of NPTT in real conditions. In the present study, we have developed a magnetic resonance imaging (MRI)-based numerical modeling strategy for simulation and treatment planning of NPTT. To this end, we have utilized the core-shell γ-Fe$_2$O$_3$@Au nanoparticle comprising a gold layer with plasmonic properties and a magnetic core that enables to track the location of this structure via MRI. The map of nanoparticle distribution in the tumor derived from T$_2$-weighted MR image was imported into a finite element simulation software, and Pennes bioheat equation and Arrhenius damage model were applied to simulate the temperature and damage distributions, respectively. The validation of the model developed herein was assessed by monitoring the superficial and the central temperature variations of the tumor in experiment. Both the numerical modeling and experimental study proved that a localized heating and then a focused damage could be achieved due to nanoparticle inclusion. There is quite satisfactory agreement between the numerical and experimental results. The model developed in this study has a good capability to be used as a promising planning method for NPTT of cancer.

1. Introduction

Traditional cancer therapy modalities including surgery, chemotherapy and radiotherapy suffer from serious limitations and in many cases cannot provide satisfactory therapeutic outcomes. Thermal therapy has been introduced into the clinical practice as a promising cancer therapy strategy due to its acceptable safety and negligible side effects. It can be either used as a singular therapy for thermal ablation of cancer cells (temperature above 47 °C) or as an adjunct therapy to increase the tumor cells' sensitivity toward radiotherapy and chemotherapy (temperature 40–45 °C) [1–4]. The major challenge facing the extensive use of thermal therapy in clinical practice is related to the lack of an appropriate way for selective delivery of heat to the tumor site while keeping the collateral healthy tissue from unwanted thermal damages. In conventional thermal therapy methods, as the external energy source passes through the body a temperature gradient is generated within the body, so that the thermal energy is mainly deposited in surface tissues and instantly losses with depth. Therefore, to deliver sufficient heat to the deep-seated tumors, unwanted damage to overlying healthy tissues situated along the pass of external heat source seems to be inevitable [5].

Nanotechnology has recently created a renewed enthusiasm in cancer thermal therapy by exploiting the novel concept of nanoparticle-assisted thermal therapy. In this approach, nanoparticles are embedded within the target to absorb the energy originated from the external heat source, thereby generating localized heat within the tumor [6–8]. Nanoparticle-assisted photothermal therapy (NPTT) is the most-established nanoparticle-assisted thermal therapy approach wherein the interaction between near-infrared (NIR) laser and plasmonic nanomaterials is used to enhance the thermal deposition and selectivity

of thermal damages [9–11]. In this approach, the highest transmissivity of light in the NIR region due to its minimal interaction by the biological absorbers together with the ability of plasmonic nanoparticles to be tuned to the NIR region can realize a targeted thermal therapy strategy [12].

Recently, the use of multifunctional nanomaterials has yielded remarkable progress in cancer thermal therapy [13,14]. The core-shell structure of bimetallic iron oxide-gold nanoparticle has gained great attention in this area due to its capability to integrate the diagnostic and therapeutic potentials into a single platform. Owing to their unique thermophysical properties, gold nanoparticles (AuNPs) have been extensively used as a light-responsive nanomaterial in NPTT [15–17]. On the other hand, magnetic properties of iron oxide nanoparticles (IONPs), especially magnetite (Fe_3O_4) and maghemite (γ-Fe_2O_3), allow them to widely serve as a negative contrast agents in magnetic resonance imaging (MRI) [18]. Both magnetite and maghemite exhibit superparamagnetic behavior that allows their manipulation with external magnetic fields. However, due to its electronic structure, maghemite is the more stable polymorph of iron oxide. In addition to suitable magnetization and stability, maghemite nanoparticles are also biocompatible and potentially non-toxic, that ensure their wide application in biomedicine. Therefore, the maghemite-gold core-shell nanoparticles can realize an MRI-guided NPTT strategy wherein the gold layer responds to laser light and generates heat while the magnetic core gives the ability to track the location of this nanostructure through MRI.

Numerical modeling for simulation and treatment planning of NPTT is essential to predict the temperature distribution within the body to ensure that the tumor will receive the correct thermal dose. Furthermore, pre-treatment planning may predict hot spots and thus helps to reduce the risk of unwanted thermal damages particularly for thermally sensitive normal tissues such as the spinal cord [19–22]. Therefore, the development of a pre-treatment planning tool seems to be crucial for prediction of the temperature and damage distributions within the tumor due to NPTT. Non-invasive identification of nanoparticles distribution within the tumor tissue is a key perquisite to accurately predict the temperature and damage distributions. However, few studies have been conducted to identify the biodistribution of nanoparticles from medical imaging modalities in order to include that in numerical calculations of temperature distribution. In the present study, we have developed an MRI-based numerical modeling strategy for simulation and treatment planning of NPTT by utilizing γ-Fe_2O_3@Au core-shell nanoparticles. To this end, γ-Fe_2O_3@Au nanoparticles were injected to the CT26 colorectal tumor model and the nanoparticles distribution was tracked using MRI. The resulting map of nanoparticles distribution was imported into a finite element simulation software for photothermal simulation. Then, Pennes bioheat equation and Arrhenius damage model were used to simulate the temperature and damage distributions, respectively. Finally, the validation of the model developed herein was assessed by the comparison of the numerical calculations and experimental measurements. Fig. 1 shows the overall workflow diagram of the present study in different phases.

2. Materials and methods

2.1. Preparation and characterization of γ-Fe_2O_3@Au nanoparticles

γ-Fe_2O_3@Au nanoparticles were synthesized according to the method reported in our previous study [9]. The morphological investigation of γ-Fe_2O_3@Au nanoparticles were performed by Zeiss LEO 906 transmission electron microscope (TEM). The hydrodynamic diameter of nanoparticles in water was determined by dynamic light scattering (DLS), Malvern Zetasizer Nano ZS-90 instrument. The zeta potential indicating the surface charge of nanoparticles was also measured by the DLS instrument. To determine the light absorption peak of nanoparticles, UV–Visible (UV–Vis) absorption spectra were recorded using a Rayleigh UV- 1601 instrument.

2.2. Cell culture and tumor induction

CT26 cell line, derived from mouse colon adenocarcinoma, was obtained from Pasteur Institute of Iran. Cells were grown in RPMI 1640 medium with 10% FBS, 100 units/ml penicillin, and 100 μg/ml streptomycin at 37 °C in 5% CO_2. Cells were harvested by trypsinizing cultures with 1 mM EDTA/0.25% Trypsin (w/v) in PBS. After three passages, cells were counted and resuspended in a medium solution at a concentration of ten millions per milliliter for tumor inoculation.

Male Balb/c mice (5–8 weeks old, 20–25 g) were obtained from Pasteur Institute of Iran. Animals were housed under controlled light, temperature, and humidity conditions for 1 week before use. All animal experiments were conducted in accordance with guidelines established by institutional animal Care Committee. Two million CT26 cells suspended in their culture medium were injected subcutaneously on the right flank of Balb/c mice. The experiments were started when the tumor volume grew to approximately 150 mm^3.

2.3. Remote detection of nanoparticles distribution by MRI

Due to their magnetic core, γ-Fe_2O_3@Au nanoparticles can generate contrast in MR images, thus endowing the ability to track them via MRI. To this end, tumor-bearing mice were imaged before nanoparticle injection to reveal the baseline level of soft tissue image contrast (Fig. 2a). Next, 30 μl of γ-Fe_2O_3@Au nanoparticles (Au concentration: 50 ppm) were injected directly into the center of the tumor and the mice were imaged 30 min post-injection. The MRI study was performed by using Philips superconductor clinical MR system (1.5 T) with the following acquisition parameters:

$T_2 *$ weighted gradient echo, TR: 250 ms, TE: 11 ms, FA

: 25 and slice thickness 2 mm

The resultant T_2-weighted MR images indicated a clear distinction between nanoparticles and soft tissue (Fig. 2b). MR images were processed in MATLAB prior to being imported into finite element simulation software. Images were segmented for quantification of MR signals before and after injection (Fig. 2c and d). Then, a single fixed threshold signal intensity was set manually based on the difference in the signal intensity of the tumor before and after injection of nanoparticles in order to determine nanoparticle distribution contour. This step was performed to distinguish nanoparticles from the tumor tissue in MATLAB. Subsequently, a gradient edge detection filter was applied to identify mouse body contour (Fig. 2e). Then, the geometry model was imported into COMSOL Multiphysics® modeling software (version 5.2) for photothermal simulations. The geometry model was meshed with non-uniform size and shape grids (Fig. 2f), and finite element simulation was then carried out for each element separately [23].

2.4. Modeling of temperature and damage distributions within the tumor

Fig. 3 shows the schematic of model geometry for simulating the temperature and thermal damage distributions. The computational modeling was performed in three steps: 1) calculation of light distribution in the tumor tissue using photon diffusion equations, 2) determination of temperature distribution within the tumor based on the Pennes bioheat transfer equation, and 3) estimation of tissue damage based on the Arrhenius relationship.

2.4.1. Laser heating model

When a laser beam propagates through the tissue, it will be absorbed and scattered depending upon the absorption and scattering coefficients of the medium. The radiative transport theory was employed to model the light field distribution within the tissue [24,25].
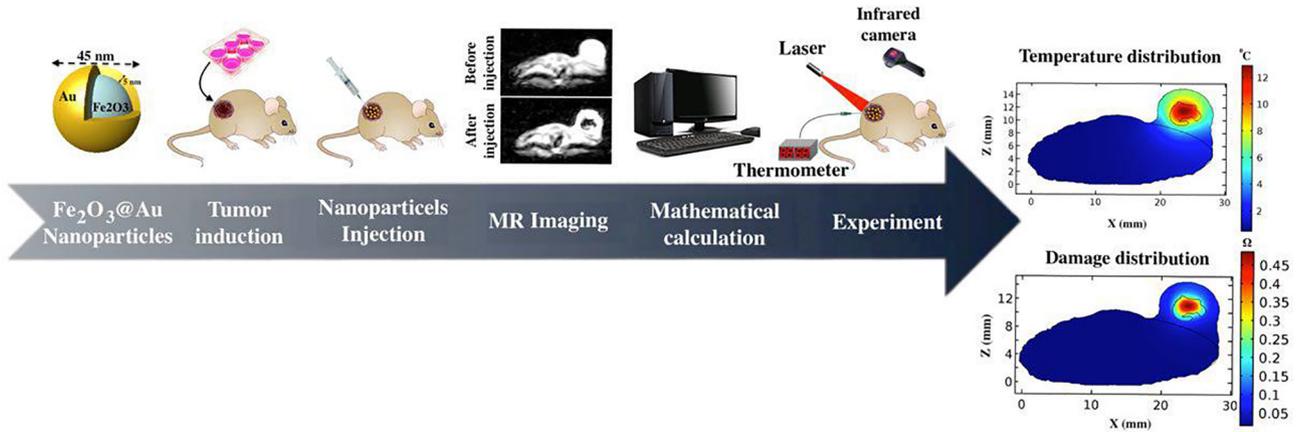
Fig. 1. Schematic workflow diagram of the present study.

According to this theory, light diffusion in the tissue can be determined by the following approximation:

$$-D\nabla^2\varphi(r, t) + \mu_a\varphi(r, t) = s(r, t) \tag{1}$$

where $\varphi(r, t)$ is the light fluence rate (W/m^2), $s(r, t)$ is the source term (W/m^3), t is time (s), r is Cartesian coordinate (m), and D is the diffusion coefficient (m) given by:

$$D = \frac{1}{3(\mu_s' + \mu_a)} \tag{2}$$

where μ_a is the absorption coefficient and $\mu_s' = \mu_s(1 - g)$ is the reduced scattering

coefficient. μ_s is scattering coefficient and g is the anisotropy factor which is typically chosen as > 0.9 for most tissues, implying that most scattering events result in forwarding motion of photons.

When the plasmonic nanoparticles are impregnated into the tissue, they alter the optical properties of the medium. The total absorption (μ_{atot}) and reduced scattering (μ_{stot}') coefficients of a tissue due to the embedded nanoparticles can be calculated as follows [26]:

$$\mu_{atot} = \mu_{at} + 0.75 f_v \frac{\sigma_a}{a} \tag{3}$$

$$\mu_{stot}' = \mu_{st}' + 0.75 f_v \frac{\sigma_s'}{a} \tag{4}$$

where μ_{at} and μ_{st}' are the absorption and reduced scattering coefficients of tissue. f_v is the volume fraction of the nanoparticles, σ_a and σ_s' stand for the dimensionless efficiency factor of absorption and transport efficiency factor of scattering for single nanoparticles, respectively. a represents the nanoparticles radius. Therefore, the presence of plasmonic nanoparticles within the tissue can increase the total absorption and scattering coefficients, which in turn alters the thermal distribution due to the increased value of φ in Eq. (1).

Fig. 3. Schematic of model geometry showing the 2D cross-sectional view of a tumor-bearing mouse irradiated by laser.

2.4.2. Bioheat transfer model

After determining the light distribution in the tumor tissue embedded with nanoparticles using the diffusion approximation of the transport theory, the resulting temperature distribution was modeled using the Pennes bioheat equation [27]:

$$\rho c \frac{\partial T(r, t)}{\partial t} = \nabla(k\nabla T(r, t)) + Q_s + Q_p + Q_m \tag{5}$$

where ρ, c and k are the density, specific heat and thermal conductivity of the tissue, and $Q_p = \rho_b c_b \omega_b(T_b - T)$ is the heat gained or lost due to blood perfusion, where ω_b, ρ_b, c_b, and T_b are blood perfusion rate, blood density, specific heat and temperature of blood, respectively. Q_m is the heat generated due to metabolic activity, and Q_s is the heat generated
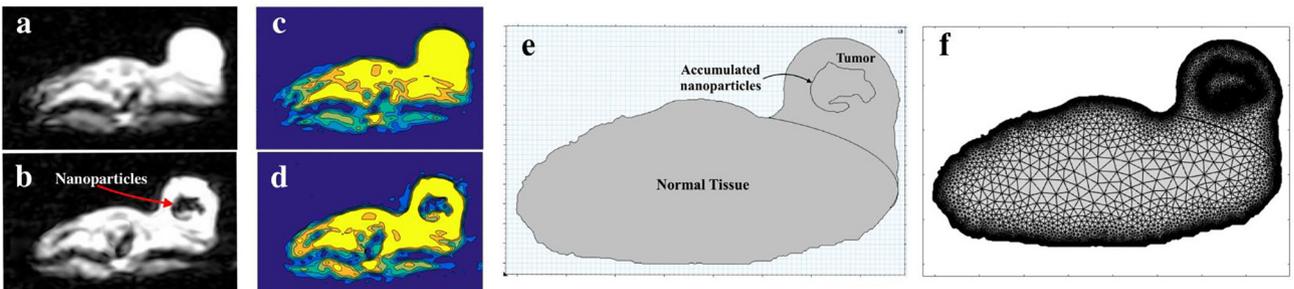

Fig. 2. Steps of image processing for model generation. (a, b) MR images of the tumor-bearing mouse before and after nanoparticles injection. (c, d) Segmented MR images before and after nanoparticle injection. (e) Defining the outer contour of mouse body and the inner contour of nanoparticle distribution. (f) Configuring meshes in COMSOL software.
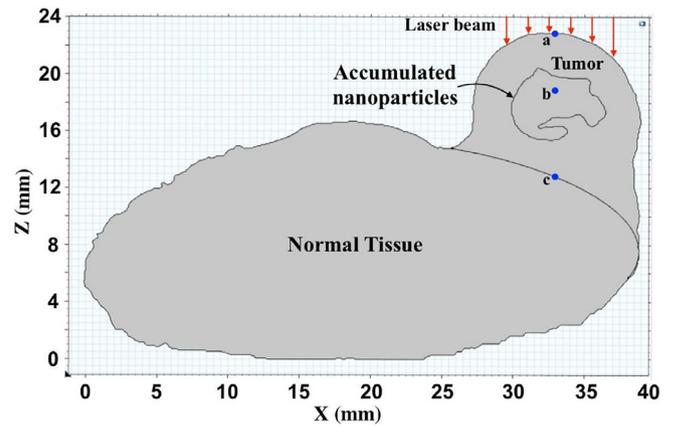
due to NPTT and can be expressed as [24]:

$$Q_s(r, t) = \mu_a \varphi(r, t) \ (\text{W/m}^3) \tag{6}$$

To consider heat transfer at the boundary between the surface of the mouse body and air due to the convection mechanism, a Neumann boundary condition was applied, given by [24]:

$$-k\frac{\partial T}{\partial n} = h(T_b - T_\infty) \tag{7}$$

where h is the convective transfer coefficient, n is the unit outward normal, T_b and T_∞ are the temperature at the boundary and the ambient temperature of the environment (24 °C), respectively.

2.4.3. Thermal damage model

The Arrhenius relationship was applied in order to simulate the irreversible thermal damages due to the photothermal heating [28]. According to this model, the thermal damages can be expressed in the form of a dimensionless parameter, Ω, representing the thermal damage rate [29]:

$$\Omega(t) = \int Ae^{\frac{-E_a}{RT(t)}}dt \tag{8}$$

where E_a and A are the activation energy (J/mol) and the frequency factor (s^{-1}), respectively. R is the gas constant which equals to 8.314 J/(mol K). T and t stand for the absolute temperature of tissue and duration of heat exposure, respectively. Table 1 represents the numerical values of the thermal and optical characteristics of the tissue and γ-Fe$_2$O$_3$@Au nanoparticles used for model simulation in this study.

2.5. Thermometry and experimental validation

CT26 tumor-bearing mice injected with γ-Fe$_2$O$_3$@Au nanoparticles were irradiated with a continuous-wave 808 nm NIR laser source (Nanobon Company, Tehran, Iran) at a power density of 5 W/cm^2 for 3 min. Before laser irradiation, a thermocouple probe (with diameter of 125 µm) was inserted at the center of the tumor using a syringe needle to monitor the transient temperature variations. Simultaneously, the superficial temperature of the tumor was also recorded with an infrared (IR) thermal camera (Testo 875–1i, Germany). Fig. 4 shows the schematic illustration of experimental set up.

3. Results

3.1. Characterization of γ-Fe$_2$O$_3$@Au nanoparticles

The morphological characteristic of γ-Fe$_2$O$_3$@Au nanoparticles was investigated by TEM. Fig. 5a displays a TEM image of γ-Fe$_2$O$_3$@Au nanoparticles, wherein the core-shell structure can be clearly observed. The magnetic core of γ-Fe$_2$O$_3$@Au nanoparticles has a diameter of ~35 nm and a gold layer of ~5 nm thick covers the magnetic core. The hydrodynamic size distribution of γ-Fe$_2$O$_3$@Au nanoparticles measured

by DLS analysis is presented in Fig. 5b. Accordingly, the effective diameter of the nanoparticles ranges between 25 and 75 nm, with the highest frequency at 50 nm. The zeta potential that reflects the dispersion stability of γ-Fe$_2$O$_3$@Au nanoparticles was −22.4 mV (Fig. 5c). Given that nanoparticle suspensions with zeta potential values of ± 20–30 mV are classified as moderately stable [32], the stability of γ-Fe$_2$O$_3$@Au nanoparticles can be considered as such. Moreover, the UV–Vis spectrum was also recorded to confirm the formation of a complete core–shell structure (Fig. 5d) [33]. Compared to 50 nm AuNPs, a red shift and broadening of the peak can be seen in the absorption spectra of γ-Fe$_2$O$_3$@Au nanoparticles.

3.2. Estimation of temperature distribution

After determining the localization of γ-Fe$_2$O$_3$@Au nanoparticles within the tumor tissue by MRI, the model geometry was generated in COMSOL. Two-dimensional finite element simulations were conducted to investigate the effect of nanoparticles inclusion on the temperature distribution of the tumor during laser irradiation. Fig. 6 shows the temperature distribution map on a transverse cross-section of the mouse body as a result of NIR laser irradiation at a power density of 5 W/cm^2 for 3 min. It is apparent that the presence of γ-Fe$_2$O$_3$@Au nanoparticles can significantly alter the temperature distribution pattern within the tumor tissue. The tumor without nanoparticles inclusion indicates a clear temperature gradient with the maximum value at the surface (skin) that steadily decreases with depth. In contrast, the tumor embedded with nanoparticles exhibits an inside-out temperature gradient pattern during laser irradiation, wherein the maximum temperature occurs at the accumulation site of nanoparticles in the tumor core.

Fig. 7 represents a detailed graph about how the presence of γ-Fe$_2$O$_3$@Au nanoparticles alter the temperature distribution within the tumor. Fig. 7a shows the temperature rise profile as a function of time at various depths of 0, 3.5 and 10 mm along the central axis of the tumor with and without nanoparticles inclusion. As shown in Fig. 7a, after 3 min laser irradiation, the maximum temperature rise for the tumor without nanoparticles is only ~3 °C which is obtained at the surface (Z = 0), whereas the tumor embedded with nanoparticles shows a maximum temperature rise of ~13 °C at a point 3.5 mm deep (point b) along the central axis of the tumor. Fig. 7b shows the temperature rise profile as a function of depth at various exposure times along the central axis of the tumor with and without nanoparticles inclusion. Compared to the tumor without nanoparticles, the point of maximum temperature rise lies deeper into the tissue for the tumor embedded with nanoparticles, and the superficial temperature is notably lower than the maximum temperature.

3.3. Prediction of thermal damage

Enhanced thermal deposition due to the injection of γ-Fe$_2$O$_3$@Au nanoparticles is expected to cause a dramatic increase in the damage of

Table 1
Symbols and values of the parameters considered in this study [30,31].

| Thermal properties		Optical properties	
Parameter	Value	Parameter	Value
density of tissue and blood, ρ and ρ_b	1052 kg/m^3	absorption coefficient, μ_{at}	0.8 cm^{-1}
specific heat of tissue and blood, c and c_b	3800 J/kg.K	scattering coefficient, μ_{st}	100 cm^{-1}
thermal conductivity, k	0.5 W/mK	absorption coefficient, μ_{atot}	1.8 cm^{-1}
blood perfusion, ω_b	0.01 s^{-1}	scattering coefficient, μ_{stot}	100.01 cm^{-1}
blood temperature, T_b	37 °C	anisotropy factor, g	0.9
metabolic activity, Q_m	40 kW/m^3		
convective coefficient, h	10 W/m^2.K		
activate energy, E_a	7.39E + 39 J/mol		
frequency factor, A	2.50E + 05 s^{-1}		
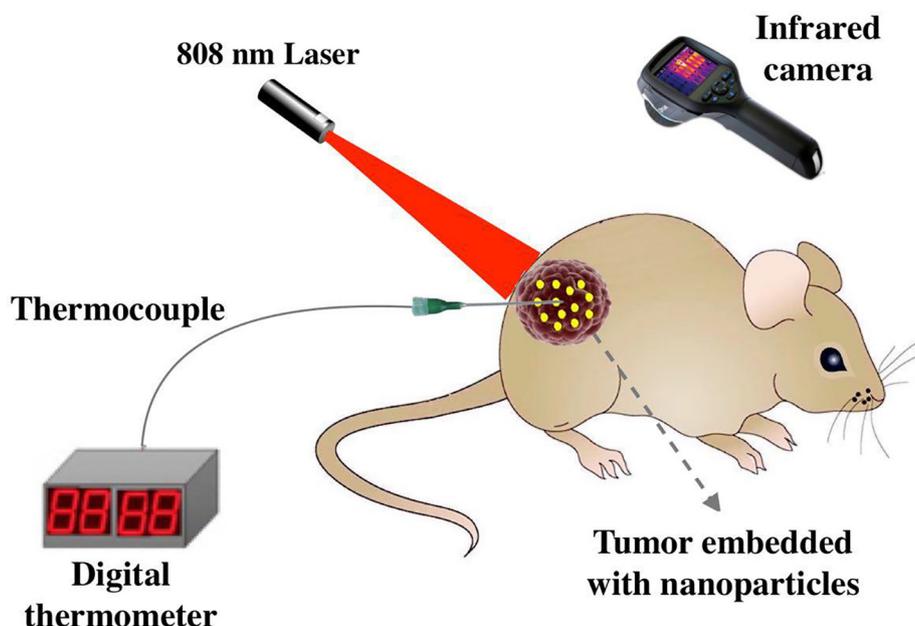
Fig. 4. Schematic illustration of experimental set up.

the tumor containing nanoparticles as compared to the tumor without nanoparticles. To test this proposition, the Arrhenius damage model was used to simulate the thermal damages caused by photothermal induction. Fig. 8 compares the damage distribution induced by laser irradiation (5 W/cm², 3 min) to the tumor with and without the injection of γ-Fe₂O₃@Au nanoparticles. As expected from temperature distribution data, a completely negligible damage occurred in the tumor without nanoparticles, whereas the central region of the tumor embedded with nanoparticles was significantly injured. Fig. 9a and b show

the fraction of thermal damage (necrosis) as a function of time and depth along the central axis of the tumor, respectively. These figures suggest that the presence of nanoparticles can shift the thermal damages deposition to the deeper regions of tissue while the surface regions of tissue is spared.

3.4. Model validation

In order to validate the current developed model, the computational
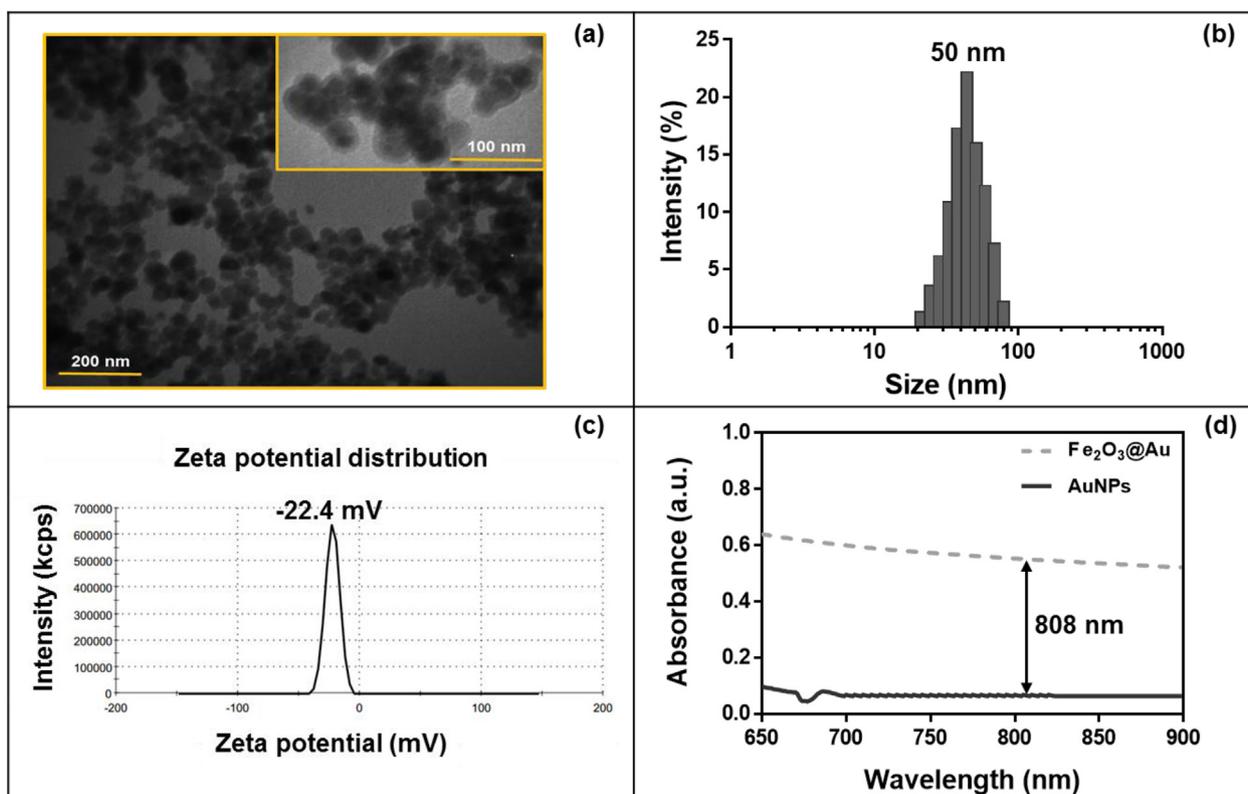

Fig. 5. Nanoparticle characterization. (a) TEM image (arrows indicates Au shell), (b) hydrodynamic size distribution, (c) zeta potential distribution and (d) UV–Vis absorption spectra of γ-Fe₂O₃@Au nanoparticles in comparison with 50 nm AuNPs.
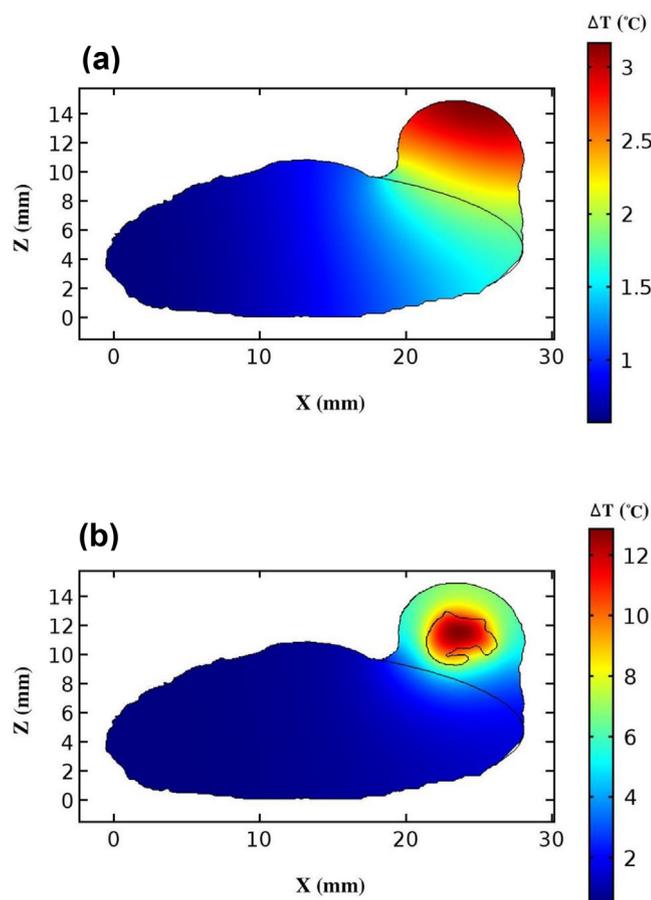
Fig. 6. 2D transverse cross-section view of the mouse body showing temperature distribution map (a) with and (b) without injection of γ-Fe$_2$O$_3$@Au nanoparticles, after NIR laser irradiation (5 W/cm^2, 3 min).

Fig. 7. Temperature profiles as a function of time (a) at various depth points (points a, b and c in Fig. 3 that correspond to depths of 0, 3.5 and 10 mm, respectively) and as a function of depth (b) at various laser exposure times (30, 60 and 120 s) along the central axis of the tumor with and without nanoparticle inclusion. ΔT represents the temperature rise of tumor due to laser irradiation.

results and the experimental measurements for spatiotemporal temperatures were compared. To this end, both the superficial and the central temperature variations of the tumor were recorded by a thermal camera and a thermocouple inserted into the tumor (as shown in Fig. 4). Fig. 10a and b compare the numerical calculations with the experimental data from the perspectives of the superficial and the central temperature variations of the tumor, respectively. As can be seen, the measurement data also exhibit a large difference between the superficial and the central temperature due to the injection of γ-Fe$_2$O$_3$@Au nanoparticles as observed in the numerical simulation. Taken together, these results suggest that there is quite satisfactory agreement between the numerical and experimental results, where the measured temperatures are within 5% of simulation results.

4. Discussion

As a non-invasive or minimally invasive technique, hyperthermia is suggested an alternative treatment option to treat solid tumors. Different energy sources are currently employed in clinical practice for tumor hyperthermia including laser, microwaves, radiofrequency waves and ultrasound. The penetration depth of laser in tissue is highly limited due to strong absorption of light by tissue compositions, such as hemoglobin and melanin. The optimal wavelength window for deeper penetration of light is in the NIR region (700–1100 nm) where light has minimal interaction with biological absorbers. This limited penetration depth of light restricts the application of laser-induced hyperthermia to the superficial or endoscopically accessible tumors. On the contrary, microwaves, radiofrequency waves and ultrasound are able to circumvent this barrier, offering a suitable hyperthermia source for
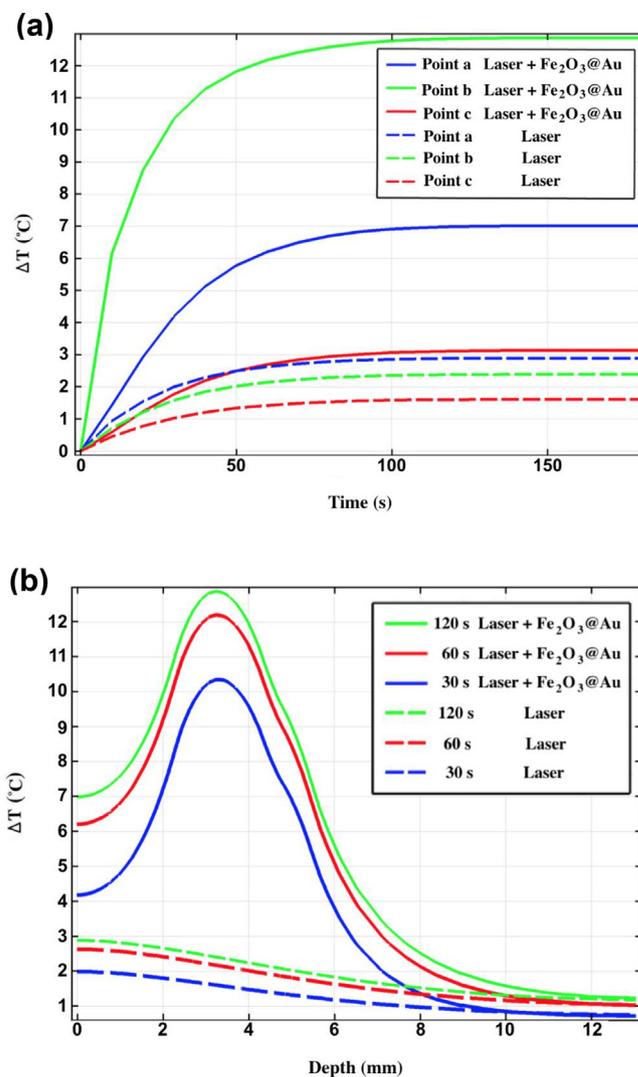
thermoablation of deep-seated tumors. However, laser-induced hyperthermia provides remarkable benefits over other thermal therapy modalities. It offers a more efficient, economical and safer strategy thanks to the technological advancement in laser delivery equipment, such as actively cooled applicators and high power diode lasers. Laser-induced hyperthermia also enables a superior selectivity in heat delivery with more control over perfusion effects and a significantly shorter treatment duration relative to other thermal therapy modalities. Laser does not require a complicated setup and can be easily coupled with imaging devices (e.g., MRI), with minimal induced image artifacts. Moreover, in recent years, light-responsive nanomaterials have shown tremendous promise to expand the clinical utility of laser hyperthermia through enhancing the selectivity of thermal damages [2,34].

Despite the promising pre-clinical evidences, NPTT encounters with serious challenges that should be addressed before clinical translation. Monitoring temperature during thermal therapy operation is not currently feasible. Invasive thermometry only offers sporadic and unreliable temperature information and also increases the risk of complications [35]. Non-invasive magnetic resonance imaging thermometry (MRIT) that provides real time 3D temperature mapping also has following limitations: it is costly, not widely available, not applicable for
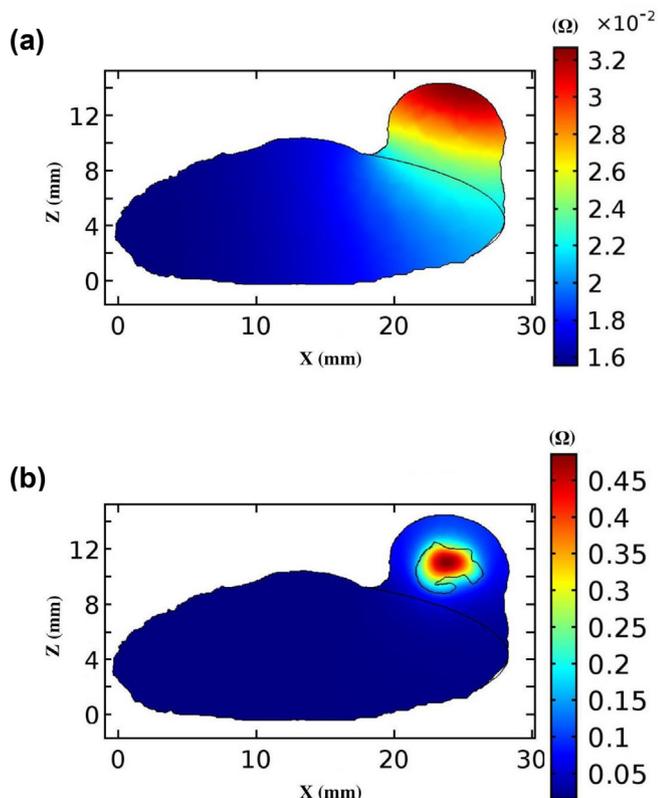
Fig. 8. 2D transverse cross-section view of the mouse body showing thermal damage distribution map (a) with and (b) without injection of γ-Fe$_2$O$_3$@Au nanoparticles, after NIR laser irradiation (5 W/cm^2, 3 min). $\Omega = 1$ indicates complete necrosis of the tissue and irreversible thermal damage.

Fig. 9. Thermal damage profile (fraction of necrotic tissue) as a function of time (a) at various depth points (points a, b and c in Fig. 3 that correspond to depths of 0, 3.5 and 10 mm, respectively) and as a function of depth (b) at various laser exposure times (30, 60 and 120 s) along the central axis of the tumor with and without nanoparticle inclusion. $\Omega = 1$ indicates complete necrosis of the tissue and irreversible thermal damage.

all tissue types and not yet sufficiently accurate and stable [36]. However, prediction of temperature distribution and hot spots during treatment is a critical point in thermal therapy modalities. Pre-treatment planning is essential to ensure that the tumor will receive the correct thermal dose. Furthermore, the use of pre-treatment planning would help to predict and control the size of hot spots in order to reduce the risk of undesired thermal damages to normal tissues [19]. Currently, several treatment planning tools have been developed for traditional hyperthermia [37,38]. Nevertheless, the prediction of temperature distribution would be more difficult in case of nanoparticle-assisted thermal therapy methods where the inclusion of nanoparticles into the tissue and their interaction with external heat source leads to additional complexity [5].

In NPTT, the interaction between the incident laser light and plasmonic nanoparticles causes the synchronized excitation of the conduction band electrons, thus inducing strong electric fields on the surface of nanoparticles. The absorbed light is converted into heat through a series of photo-physical processes and transferred into the surrounding environment, thereby resulting in a localized intense temperature rise around the particle [39]. Therefore, accurate computational modeling of temperature distribution within the tissue due to NPTT highly depends on the understanding of nanoparticles distribution pattern in real conditions. Unfortunately, nanoparticles distribution in the tumor is not possible to predict due to heterogeneous tumor geometries, differences in tumor porosity that affects tumor penetration of nanoparticles, and the random interaction of nanoparticles with cell membrane [40]. Although, a significant number of preliminary studies have been yet carried out for simulation and treatment planning of NPTT, they have mostly employed the simple phantom models and simple patterns of nanoparticles distribution such as a uniform or a Gaussian distribution, which is far away from clinical
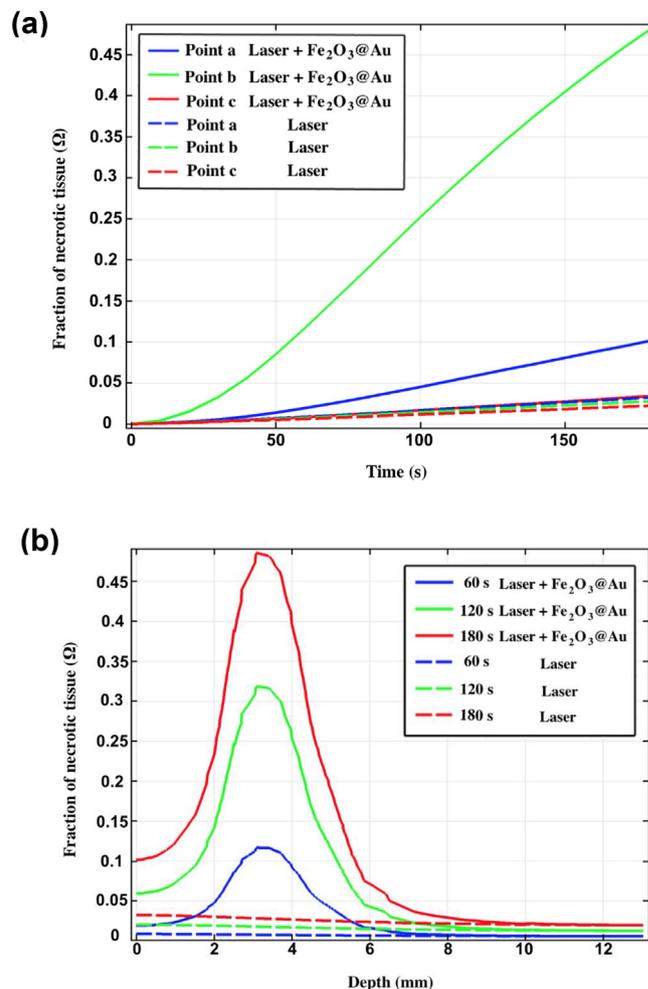
reality [41–43]. Therefore, taking into consideration the actual tumor geometry and nanoparticles localization would be a great step to enhance the accuracy and prediction power of the heat transfer simulation.

Recently, extensive efforts have been made to develop a reliable numerical modeling approach for predicting the effects of NPTT. However, in most of these efforts, the simulation results have been validated on phantoms or cells, and only few studies have investigated in vivo data sets. Furthermore, the existing in vivo-validated studies have mostly considered the superficial temperature of tumor, but lacks from interstitial temperature data. For example, Maltzahn et al. developed a computationally modeling of spatiotemporal temperature in tumor treated with PEGylated gold nanorods or gold nanoshells followed by NIR irradiation [44]. Although, non-invasive computed tomography imaging was used to determine the actual biodistribution of nanoparticles for enhancing the prediction power of the model, only the surface temperature was compared between the simulation and experimental measurement. Therefore, the present study makes a major contribution to this growing area of research by exploring experimental and modeling results for both superficial and interstitial temperature data. Only one study by Mooney et al. compared both the observed surface and internal temperature values from in vivo experiments with
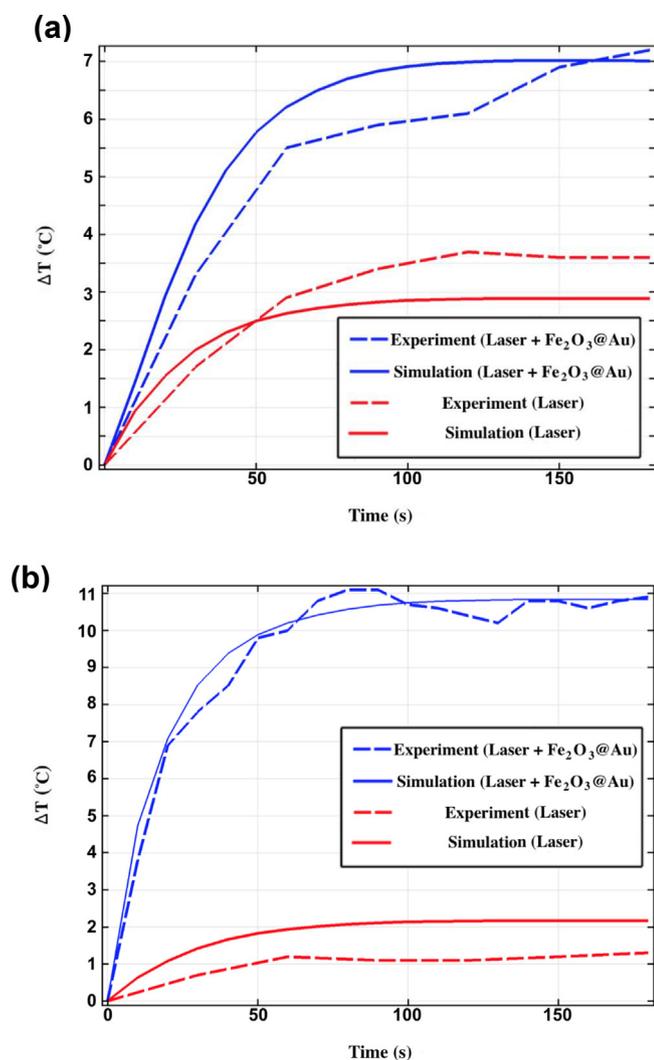
(a)

(b)

Fig. 10. Comparison of the numerical calculations with the experimental measurements of (a) the superficial and (b) the central temperature variations of the tumor during laser irradiation. *ΔT* represents the temperature rise of tumor due to laser irradiation.

the theoretical modeling. The constructed model was able to predict gold nanorods-mediated NPTT with mean temperature deviation of 1.2 °C compared to experimental observations. However, similar to most existing works, the accuracy of the model was restricted because of the lack of information about the spatial distribution of nanoparticles.

In the present study, we have developed a novel MRI-based numerical modeling for simulation and treatment planning of NPTT by utilizing multifunctional γ-Fe$_2$O$_3$@Au nanoparticles. In this strategy, the magnetic core of γ-Fe$_2$O$_3$@Au nanoparticles can help to track the nanoparticle's location via MRI which is essential for accurate prediction of temperature distribution in individual patients following NPTT. The model validation results (Fig. 10) indicated that a faster heating rate is observable in the simulations compared to practical observations, which could be attributed to the description of the blood perfusion contribution [45]. However, at the end of treatment operation, the predicted temperatures are close to the experimental measurements. The maximum and the mean temperature deviation between the simulation and experiment were 1.1 °C and 0.7 °C, respectively. These results suggest the satisfactory performance of the constructed model to predict steady-state temperature distribution in NPTT. Generally, a good correlation between the calculated and experimental temperature distribution requires multiple temperature detection points. On the

other hand, multiple temperature measurements from different depths of an individual tumor seem to be not feasible in practice. Therefore, experimental validation by using MRIT that provides a 3D temperature mapping could be a useful approach to further refine the prediction power of NPTT modeling.

Overheating of the surface tissues is a major issue due to the application of conventional thermal therapy methods. Therefore, the power density of the external heat source should be kept low in order to prevent the surface overheating problem and its resultant side effects. As a result, sufficient heat cannot be transferred to the deep areas of the body that limits the treatment of deep-seated tumors [46]. Both the computational and measurement results in this study proved that nanoparticles are able to focus the energy of laser light and generate a localized heating in their site of accumulation. Therefore, it provides the possibility to increase the temperature of deep-seated tumors by nanoparticles while keeping the surface tissue within a safe temperature range, thereby achieving a skin-sparing effect and preventing surface overheating.

5. Conclusion

The purpose of the current study was to promote a pre-treatment planning strategy for rational prediction of temperature and damage due to NPTT. The multifunctional iron oxide-gold core-shell nanoparticle is suggested as a promising agent to achieve a powerful treatment planning tool for NPTT, whereby the photothermal treatment and noninvasive assessment of nanoparticle biodistribution can be realized simultaneously. The numerical modeling in agreement with experimental results indicated that the injection of nanoparticles and subsequent laser irradiation can generate a localized heating at the site of accumulation of nanoparticles while providing a skin-sparing effect and preventing surface overheating. The model developed herein is one of the first image-based numerical modeling methods for simulation of cancer thermal therapy with assistance of nanoparticles. These findings will be of interest to cancer researchers and clinicians who may include thermal therapy in treatment planning of cancer patients.

Declaration of Competing Interest

The authors declare that they have no known competing financial interests or personal relationships that could have appeared to influence the work reported in this paper.

References

[1] van der Zee J. Heating the patient: a promising approach? Ann Oncol 2002;13:1173–84.
[2] Beik J, Khateri M, Khosravi Z, Kamrava SK, Kooranifar S, Ghaznavi H, et al. Gold nanoparticles in combinatorial cancer therapy strategies. Coord Chem Rev 2019;387:299–324.
[3] Mirrahimi M, Khateri M, Beik J, Ghoreishi FS, Dezfuli AS, Ghaznavi H, et al. Enhancement of chemoradiation by co-incorporation of gold nanoparticles and cisplatin into alginate hydrogel. J Biomed Mater Res B 2019.
[4] Fathy MM, Mohamed FS, Elbialy N, Elshemey WM. Multifunctional Chitosan-Capped Gold Nanoparticles for enhanced cancer chemo-radiotherapy: an invitro study. Phys Med 2018;48:76–83.
[5] Beik J, Abed Z, Ghoreishi FS, Hosseini-Nami S, Mehrzadi S, Shakeri-Zadeh A, et al. Nanotechnology in hyperthermia cancer therapy: from fundamental principles to advanced applications. J Control Release 2016;235:205–21.
[6] Chatterjee DK, Diagaradjane P, Krishnan S. Nanoparticle-mediated hyperthermia in cancer therapy. Ther Deliv 2011;2:1001–14.
[7] Beik J, Shiran MB, Abed Z, Shiri I, Ghadimi-Daresajini A, Farkhondeh F, et al. Gold nanoparticle-induced sonosensitization enhances the antitumor activity of ultrasound in colon tumor-bearing mice. Med Phys 2018;45:4306–14.
[8] Alamzadeh Z, Beik J, Mahabadi VP, Ardekani AA, Ghader A, Kamrava SK, et al.

Ultrastructural and optical characteristics of cancer cells treated by a nano-technology based chemo-photothermal therapy method. J Photochem Photobiol B 2019;192:19–25.

[9] Mirrahimi M, Hosseini V, Kamrava SK, Attaran N, Beik J, Kooranifar S, et al. Selective heat generation in cancer cells using a combination of 808 nm laser ir-radiation and the folate-conjugated Fe2O3@ Au nanocomplex. Artif Cells Nanomed Biotechnol 2017:1–13.

[10] Zeinizade E, Tabei M, Shakeri-Zadeh A, Ghaznavi H, Attaran N, Komeili A, et al. Selective apoptosis induction in cancer cells using folate-conjugated gold nano-particles and controlling the laser irradiation conditions. Artif Cells Nanomed Biotechnol 2018:1–13.

[11] Mirrahimi M, Abed Z, Beik J, Shiri I, Dezfuli AS, Mahabadi VP, et al. A thermo-responsive alginate nanogel platform co-loaded with gold nanoparticles and cis-platin for combined cancer chemo-photothermal therapy. Pharmacol Res 2019;143:178–85.

[12] Qin Z, Bischof JC. Thermophysical and biological responses of gold nanoparticle laser heating. Chem Soc Rev 2012;41:1191–217.

[13] Mieszawska AJ, Mulder WJ, Fayad ZA, Cormode DP. Multifunctional gold nano-particles for diagnosis and therapy of disease. Mol Pharm 2013;10:831–47.

[14] Abadeer NS, Murphy CJ. Recent progress in cancer thermal therapy using gold nanoparticles. The J Phys Chem C 2016;120:4691–716.

[15] Beik J, Khademi S, Attaran N, Sarkar S, Shakeri-Zadeh A, Ghaznavi H, et al. A nanotechnology-based strategy to increase the efficiency of cancer diagnosis and therapy: folate-conjugated gold nanoparticles. Curr Med Chem 2017;24:4399–416.

[16] Pan L, Liu J, Shi J. Nuclear-targeting gold nanorods for extremely low NIR activated photothermal therapy. ACS Appl Mater Interfaces 2017;9:15952–61.

[17] Samadian H, Hosseini-Nami S, Kamrava SK, Ghaznavi H, Shakeri-Zadeh A. Folate-conjugated gold nanoparticle as a new nanoplatform for targeted cancer therapy. J Cancer Res Clin Oncol 2016;142:2217–29.

[18] Eyvazzadeh N, Shakeri-Zadeh A, Fekrazad R, Amini E, Ghaznavi H, Kamrava SK. Gold-coated magnetic nanoparticle as a nanotheranostic agent for magnetic re-sonance imaging and photothermal therapy of cancer. Lasers Med Sci 2017;32:1469–77.

[19] Wiersma J, Van Wieringen N, Crezee H, Van Dijk J. Delineation of potential hot spots for hyperthermia treatment planning optimisation. Int J Hyperth 2007;23:287–301.

[20] Moros E. Physics of thermal therapy: fundamentals and clinical applications. CRC Press; 2012.

[21] Dewhirst MW, Abraham J, Viglianti B. Evolution of thermal dosimetry for appli-cation of hyperthermia to treat cancer. Adv Heat Transfer Elsevier 2015:397–421.

[22] Beik J, Asadi M, Khoei S, Laurent S, Abed Z, Mirrahimi M, et al. Simulation-guided photothermal therapy using MRI-traceable iron oxide-gold nanoparticle. J Photochem Photobiol B 2019:111599.

[23] Topaloglu U, Yan Y, Novak P, Spring P, Suen J, Shafirstein G. Virtual thermal ab-lation in the head and neck using Comsol MultiPhysics. Proceedings of the COMSOL Conference. 2008. p. 1–7.

[24] Cheong SK, Krishnan S, Cho SH. Modeling of plasmonic heating from individual gold nanoshells for near-infrared laser-induced thermal therapy. Med Phys 2009;36:4664–71.

[25] Iizuka MN, Vitkin IA, Kolios MC, Sherar MD. The effects of dynamic optical prop-erties during interstitial laser photocoagulation. Phys Med Biol 2000;45:1335.

[26] Ren Y, Qi H, Chen Q, Ruan L. Thermal dosage investigation for optimal temperature distribution in gold nanoparticle enhanced photothermal therapy. Int J Heat Mass Transf 2017;106:212–21.

[27] Pennes HH. Analysis of tissue and arterial blood temperatures in the resting human forearm. J Appl Physiol 1948;1:93–122.

[28] Wright NT. On a relationship between the Arrhenius parameters from thermal da-mage studies. J Biomech Eng 2003;125:300–4.

[29] Patel NV, Jethwa PR, Shetty A, Danish SF. Does the real-time thermal damage es-timate allow for estimation of tumor control after MRI-guided laser-induced thermal therapy? Initial experience with recurrent intracranial ependymomas. J Neurosurg Pediatr 2015;15:363–71.

[30] Melo AR, Loureiro MMS, Loureiro F. Blood perfusion parameter estimation in tu-mors by means of a genetic algorithm. Procedia Comput Sci 2017;108:1384–93.

[31] Soni S, Tyagi H, Taylor RA, Kumar A. Experimental and numerical investigation of heat confinement during nanoparticle-assisted thermal therapy. Int Commun Heat Mass 2015;69:11–7.

[32] Bhattacharjee S. DLS and zeta potential–what they are and what they are not? J Control Release 2016;235:337–51.

[33] Cheng G, Walker ARH. Synthesis and characterization of cobalt/gold bimetallic nanoparticles. J Magn Magn Mater 2007;311:31–5.

[34] Mooney R, Schena E, Saccomandi P, Zhumkhawala A, Aboody K, Berlin JM. Gold nanorod-mediated near-infrared laser ablation: in vivo experiments on mice and theoretical analysis at different settings. Int J Hyperth 2017;33:150–9.

[35] van der Zee J, Peer-Valstar JN, Rietveld PJ, de Graaf-Strukowska L, van Rhoon GC. Practical limitations of interstitial thermometry during deep hyperthermia. Int J Radiat Oncol Biol Phys 1998;40:1205–12.

[36] Van Rhoon GC, Wust P. Introduction: non-invasive thermometry for thermotherapy. Int J Hyperth 2005;21:489–95.

[37] Wiersma J, Van Dijk J. RF hyperthermia array modelling; validation by means of measured EM-field distributions. Int J Hyperth 2001;17:63–81.

[38] Wust P, Beck R, Berger J, Fähling H, Seebass M, Wlodarczyk W, et al. Electric field distributions in a phased-array applicator with 12 channels: measurements and numerical simulations. Med Phys 2000;27:2565–79.

[39] Myroshnychenko V, Rodríguez-Fernández J, Pastoriza-Santos I, Funston AM, Novo C, Mulvaney P, et al. Modelling the optical response of gold nanoparticles. Chem Soc Rev 2008;37:1792–805.

[40] LeBrun A, Ma R, Zhu L. MicroCT image based simulation to design heating proto-cols in magnetic nanoparticle hyperthermia for cancer treatment. J Therm Biol 2016;62:129–37.

[41] Feng Y, Rylander M, Bass J, Oden J, Diller K. Optimal design of laser surgery for cancer treatment through nanoparticle-mediated hyperthermia therapy. NSTI-Nanotech 2005:39–42.

[42] Ekici O, Harrison R, Durr N, Eversole D, Lee M, Ben-Yakar A. Thermal analysis of gold nanorods heated with femtosecond laser pulses. J Phys: D Appl Phys 2008;41:185501.

[43] Kannadorai RK, Liu Q. Optimization in interstitial plasmonic photothermal therapy for treatment planning. Med Phys 2013;40.

[44] Von Maltzahn G, Park J-H, Agrawal A, Bandaru NK, Das SK, Sailor MJ, et al. Computationally guided photothermal tumor therapy using long-circulating gold nanorod antennas. Cancer Res 2009;69:3892–900.

[45] Soni S, Tyagi H, Taylor RA, Kumar A. The influence of tumour blood perfusion variability on thermal damage during nanoparticle-assisted thermal therapy. Int J Hyperth 2015;31:615–25.

[46] Singh R, Das K, Mishra SC, Okajima J, Maruyama S. Minimizing tissue surface overheating using convective cooling during laser-induced thermal therapy: a nu-merical study. J Therm Sci Eng Appl 2016;8:011002.